The Breakdown of Single-Crystal Solidification in High Refractory Nickel-Base Alloys

T.M. POLLOCK and W.H. MURPHY

The breakdown of single-crystal solidification has been studied over a wide range of solidification conditions in ten superalloys with large variations in Re, Ta, and W content. Over the range of experimental conditions investigated, grain defect formation was sensitive to local thermal *and* solutal conditions. For a fixed alloy composition and withdrawal rate, the transition from single-crystal to equiaxed solidification did not occur abruptly. Instead, as thermal gradients were decreased in a series of experiments, isolated, highly misoriented columnar grains with the same composition as that of the base alloy developed in the presence of positive (stabilizing) thermal gradients with increasing frequency until the advance of the single-crystal front was completely blocked. The onset of columnar grain formation occurred when the primary dendrite arm spacing exceeded a critical value, corresponding to a morphological transition in the dendritic array. The onset of "freckling" was observed at the same primary dendrite arm spacing where misoriented columnar grains began to appear. In experiments with varying levels of refractory alloy content, there was also a strong correlation between the onset of grain formation and freckle formation. These observations strongly suggest that in high refractory content superalloys, the breakdown of single-crystal solidification and the formation of misoriented grains as well as freckle-type defects are sensitively dependent on thermosolutal convection processes.

I. INTRODUCTION

TRANSITIONS in modes of solidification, from plane front to cellular, cellular to columnar dendritic, or columnar dendritic to equiaxed, have long been of interest because of the sensitive dependence of mechanical properties on the grain structures of cast materials. The transition to equiaxed solidification is of particular importance for nickel-base single crystals, since the mechanical integrity of single-crystal components such as turbine blades is dependent on the elimination of high-angle grain boundaries. Unfortunately, this transition is the most difficult to quantitatively predict, due to the complex geometry of the dendritic array and the accompanying redistribution of solute during single-crystal solidification. Furthermore, since the transition involves nucleation of new grains, it is not only essential to understand the multiple mechanisms by which equiaxed grains may nucleate, but also the conditions under which grains may subsequently grow in a process where positive thermal gradients are maintained at the solidification front.

Several mechanisms for the columnar to equiaxed transition (CET) have been suggested. Chalmers[1] proposed that the CET develops due to blockage of columnar growth by equiaxed grains that nucleate as a result of the initial contact of the melt with the cooler container walls. Winegard and Chalmers[2] proposed and Hunt[3] analytically treated the alternate situation of blockage of columnar growth by nucleation of equiaxed grains in front of the advancing dendritic front, due to constitutional supercooling. Jackson *et al.*[4] observed remelting and fragmentation of secondary dendrite arms in transparent compounds and postulated that the equiaxed zone in casting was primarily due to detachment of dendrite arms and subsequent relocation to the central supercooled region of the casting. This CET transition has recently been examined in more detail *via* numerical modeling,[5,6] but accurate predictions are still not possible due to an inadequate understanding of the nucleation events, the difficulty of incorporating convection into numerical models, and the uncertainty regarding the correct thermal and solutal boundary conditions. Also, although the underlying mechanisms of the transition to equiaxed solidification in large ingots are likely to be similar to those encountered during directional solidification of large single crystals, it is important to consider the differences in local conditions, *i.e.*, the nearly constant positive, unidirectional thermal gradient imposed during directional solidification, and the orientation of the mushy zone.

In addition to suppressing a transition to equiaxed solidification, it is also desirable to avoid the phenomenon of "freckling" during solidification of superalloy single crystals. The development of these chains of very small equiaxed grains has been studied in detail in transparent compounds, binary metallic alloys, and nickel-base superalloys.[7,8,9] In directional solidification, where the liquid melt is maintained above the solid, these "channel"-type defects develop when inversely segregating elements that alter the liquid density are progressively depleted from the interdendritic fluid in sufficient quantities to initiate a convective instability.

In this research, departures from single-crystal solidification were studied in detail for a wide range of imposed thermal gradients (G) and solidification rates (R) in a series of nickel-base single-crystal alloys. Of particular interest was the influence of varying levels of refractory alloy additions on the development of grain defects during solidi-

T.M. POLLOCK, Assistant Professor, is with the Department of Materials Science and Engineering, Carnegie Mellon University, Pittsburgh, PA 15213. W.H. MURPHY, Research Engineer, is with the Engineering Materials and Technologies Laboratories, General Electric Aircraft Engines, Cincinnati, OH 45215.

Manuscript submitted November 14, 1994.

fication. The results of detailed characterization studies on microsegregation and the various types of grain defects formed during solidification will first be given. Following this will be a discussion of the contribution of refractory alloying additions to the breakdown of single-crystal solidification with emphasis on the role of thermosolutal convection and the macroscopic conditions required for avoidance of such defects. Preliminary experimental observations discussed earlier[10] will be included here for completeness.

II. EXPERIMENTAL MATERIALS AND PROCEDURES

The experimental program was designed with two objectives: (1) to isolate the influence of alloy chemistry on the breakdown of single-crystal solidification at fixed thermal conditions and (2) to investigate the influence of varying gradients and withdrawal rates at a fixed alloy composition. To accomplish this, ten different alloys were investigated with the use of two different Bridgman-type furnaces. All crystals were solidified with a growth direction of [001].

Ten alloy compositions were selected with emphasis on varying the refractory alloy content. Since high levels of Re, Ta, and W are generally desirable for high levels of creep resistance,[11,12] large variations in the amounts of these elements were investigated. The compositions of the ten alloys are listed in Table I. To systematically investigate the influence of solute variations on grain defect formation, experiments were conducted on these ten alloys under fixed processing conditions, where the average solidification rate imposed was 0.0113 cm/s and the average thermal gradient was approximately 10 °C/cm. In addition, alloy SX-1, listed in Table I, was investigated in greater detail over a broader range of solidification conditions. To minimize variations in the interstitial content, a solute lean master heat was divided and vacuum arc remelted with the desired alloying additions to achieve the final compositions in Table I. The doped heats were then used as charges for the individual directional solidification experiments.

A laboratory scale Bridgman furnace was used to solidify individual single-crystal cylindrical bars, measuring 1.3 cm in diameter by approximately 11.5 cm in length. Ceramic molds for casting the cylindrical bars were initially charged with 0.5 kg of alloy. The alloy was melted by resistance heating to approximately 1500 °C in the upper chamber of the modified Bridgman-type furnace. The directional solidification process was then initiated and controlled by withdrawal of the mold from the hot section of the furnace through a radiation baffle. Local solidification times were measured by inserting two thermocouples through the mold directly into the melt. The relationship between dendrite arm spacing and local solidification time was measured for alloy SX-1 in a series of experiments by varying the withdrawal rates (R) and thermal gradients (G) at the solidification front through adjustments in the melt superheat and the gap between the mold and radiation baffle. Primary dendrite arm spacings were measured by sectioning normal to the [001] growth direction, counting the number of primary arms over the cross-sectional area, and calculating an average spacing, in photomicrographs with magnification 50 times. Due to the wide variation in the geometry of the dendritic arrays, all average spacings were determined assuming a square array.

Table I. Compositions of Experimental Single-Crystal Alloys

Alloy	Al	Cr	Co	Hf	Re	Ta	W	Ni
SX-1	6.0	4.5	12.5	0.16	6.3	7.0	5.8	bal
SX-2	6.1	4.5	12.5	0.15	6.5	9.0	5.8	bal
SX-3	5.7	4.0	11.5	0.12	5.0	6.0	5.0	bal
SX-4	5.7	5.0	13.5	0.12	5.0	6.0	6.5	bal
SX-5	6.3	4.0	13.5	0.18	6.5	6.0	5.0	bal
SX-6	6.3	5.0	11.5	0.18	6.5	6.0	6.5	bal
SX-7	6.3	5.0	11.5	0.12	5.0	9.0	5.0	bal
SX-8	6.3	4.0	13.5	0.12	5.0	9.0	6.5	bal
SX-9	5.7	5.0	13.5	0.18	6.5	9.0	5.0	bal
SX-10	5.7	4.0	11.5	0.18	6.5	9.0	6.5	bal

The second furnace, shown schematically earlier,[10] was a production-scale furnace capable of solidifying multiple samples located on ceramic cluster molds. The use of cluster molds permitted a larger number of samples to be solidified simultaneously under approximately constant solidification conditions. Cylindrical bars, rectangular slabs (6.35 × 0.635 × 14 cm), and solid blade-shaped samples were solidified in the production-scale furnace, while only cylindrical bars were solidified in the laboratory furnace. The configuration of the blade-shaped samples has been reported earlier.[10] The cross-sectional area of the base of the solid blade sample was approximately 3 times larger than that at the midspan of the airfoil. Although the geometry of the blade poses some thermal complexities, use of these samples permitted observation of the general solidification behavior in relatively thin and thick sections, at gradients which are representative of those required for producing actual blade components. In all cases, crystals were solidified by charging ceramic molds with alloy, superheating to the range of 1482 °C to 1565 °C, and withdrawing through a radiation baffle, which served to maintain steep thermal gradients at the solidification front. In selected experiments with blade-type samples, thermal gradients at the solidification front were measured by insertion of thermocouples through the mold walls directly into the melt. The local thermal gradients in experiments not monitored by insertion of thermocouples were then indirectly extracted by measurement of dendrite arm spacings and the use of the established cooling rate–dendrite arm spacing relationships. All experiments were conducted with a constant imposed withdrawal rate throughout the solidification process.

Liquidus and solidus temperatures for each of the experimental alloys were measured by differential thermal analysis using a Thermal Analyst 2200 system with a 1600 °C cell calibrated with pure elemental standards. These measurements involved premelting a 200-g sample in an alumina crucible. For analysis, the sample was heated and cooled at a rate of 10 °C/min in a flowing argon atmosphere. Multiple cycles were used to check for reproducibility, and the solidus and liquidus temperatures were then extracted from the heating curve.

Segregation characteristics of the solidified materials were studied with a JEOL* 733 microprobe equipped with

*JEOL is a trademark of Japan Electron Optics Ltd., Tokyo.

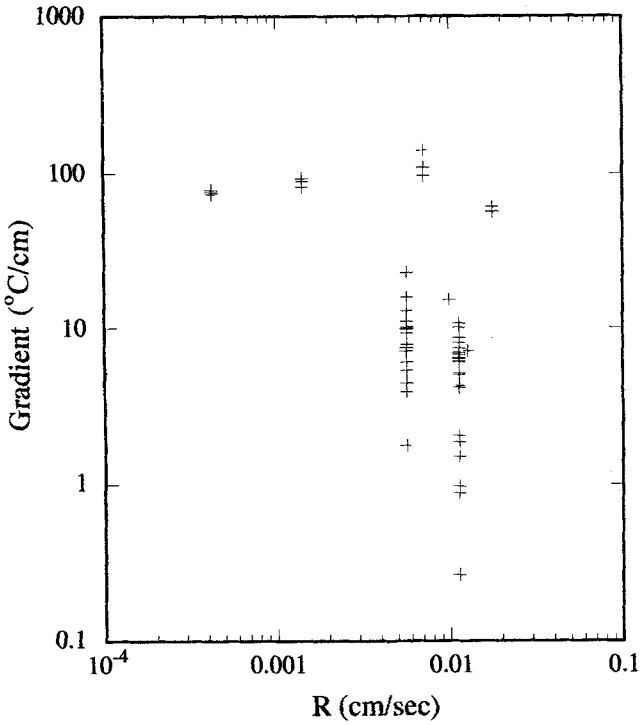

Fig. 1—Summary of experimental conditions for solidification studies conducted on alloy SX-1.

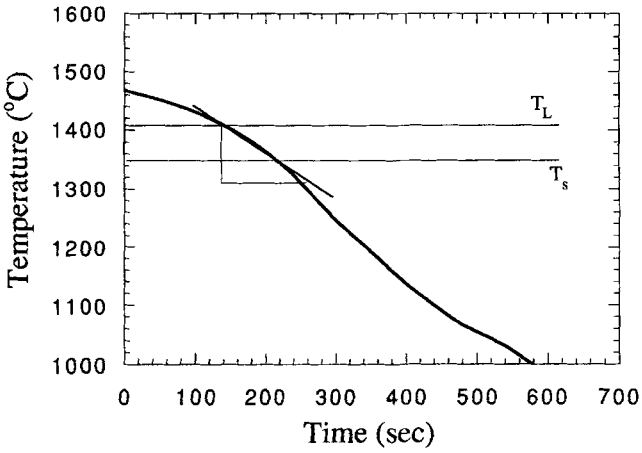

Fig. 2—Typical cooling curve obtained by inserting thermocouples directly into melt. Thermal gradients are calculated, considering solidus and liquidus temperatures from differential thermal analyses.

Table II. Results of Differential Thermal Analyses for Solidus, T_S, and Liquidus, T_L, Temperatures

Alloy	T_L, Liquidus (°C)	T_S, Solidus (°C)	$T_L - T_S$ (°C)
1	1409	1352	57
3	1436	1393	42
4	1421	1376	45
5	1429	1379	50
6	1411	1333	78
7	1401	1333	68
8	1397	1337	59
9	1407	1331	76
10	1406	1336	70

five wavelength spectrometers and a Noran 5500 stage and spectrometer automation system. Compositional variations

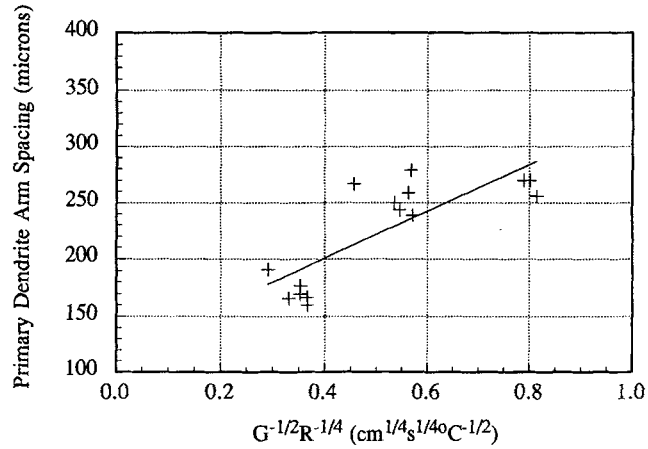

Fig. 3—The dependence of primary dendrite arm spacing on imposed processing conditions for alloy SX-1. This behavior is similar to that observed in a number of other superalloys.

from the center of the dendrite cores to the interdendritic regions were measured with a 10-μm probe analysis region.

III. RESULTS

In the first phase of this study, the influence of varying thermal gradients and solidification rates on the formation of grain defects was studied extensively with alloy SX-1. Figure 1 summarizes the experimental conditions investigated. It should be emphasized that each experimental data point in Figure 1 represents a single withdrawal experiment, but may represent more than one sample, due to the use of cluster molds with up to 14 samples per mold. In the second phase of the study, the influence of solute on the breakdown of single-crystal solidification was investigated for the remaining alloys listed in Table I. The levels of alloying elements were varied systematically to permit statistical analysis of the defect data.

A. *Alloy SX-1: Cooling Rate Experiments and Microsegregation*

The experiments on alloy SX-1 covered a wide range of process conditions, with withdrawal rates from 4.2×10^{-4} to 0.0113 cm/s and thermal gradients in the range of 0.3 to 140 °C/cm. A typical cooling curve for solidification of a cylindrical bar at a rate of 0.00706 cm/s is shown in Figure 2. The results of differential thermal analyses, given in Table II, indicated solidus and liquidus temperatures for alloy SX-1 of 1352 °C and 1408 °C, respectively. Using cooling curves such as shown in Figure 2, thermal gradients were calculated as

$$G = \left(\frac{dT}{dt}\right)\left(\frac{dt}{dx}\right) = \frac{CR}{R} \qquad [1]$$

where T is temperature, t is time, x is the distance along the long axis of the cylinder, R is the withdrawal rate, and CR is the measured cooling rate. Note that between the solidus and liquidus temperatures, the cooling curve is reasonably linear, so Eq. [1] should provide a reasonable estimate of the average gradient in the mushy zone.

In Figure 3, the measured primary dendrite arm spacings are plotted as a function of $G^{-1/2}R^{-1/4}$, based on current

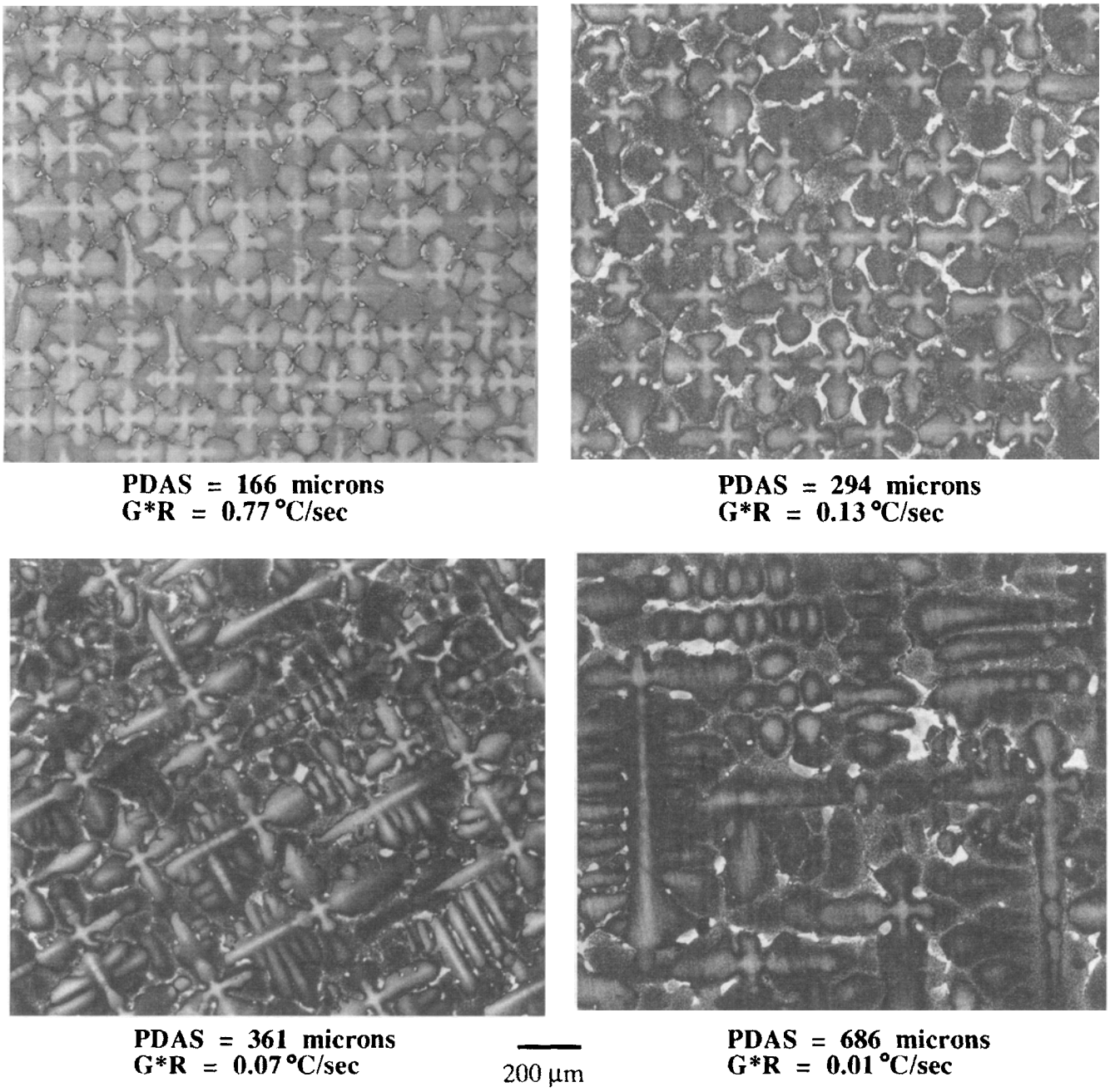

Fig. 4—The variation in primary dendrite arm spacing (PDAS) and dendrite morphology with cooling rate for alloy SX-1, viewed normal to the [001] growth direction.

theories for the development of primary arm spacings.[13,14] As for a number of other superalloys,[15] a linear relationship is observed. The dependence of the dendrite arm spacing on cooling rate for alloy SX-1 has been shown earlier,[10] and with the exception of several experiments conducted at very high thermal gradients and low solidification rates (approaching the cellular transition), there is also good agreement with a large body of data on superalloys.[15,16] In subsequent experiments, where thermocouples could not be inserted directly into the melt, the data in Figure 3, along with measurements of dendrite arm spacings, were used to indirectly determine the thermal gradients present during solidification.

The dendrite morphology as a function of cooling rate is shown in Figure 4, where samples have been sectioned normal to the solidification direction. At higher cooling rates, very regular arrays of primary dendrites develop. At lower cooling rates (low gradients), the spacing of the primary dendrites becomes somewhat irregular and extensive tertiary arm formation is apparent. The white areas in the interdendritic regions in Figure 4 are $\gamma - \gamma'$ eutectic. Figure 5 shows a section parallel to the solidification direction corresponding to the cooling curve shown in Figure 2. Well-defined secondary arms, with a spacing of approximately 40 μm, are apparent.

The results of microprobe analyses of the microstructure of as-solidified alloy SX-1 are given in Table III. Listed is the average composition of alloy SX-1 along with the composition of the material at the center of the dendrite core as well as the composition of the material in an interden-

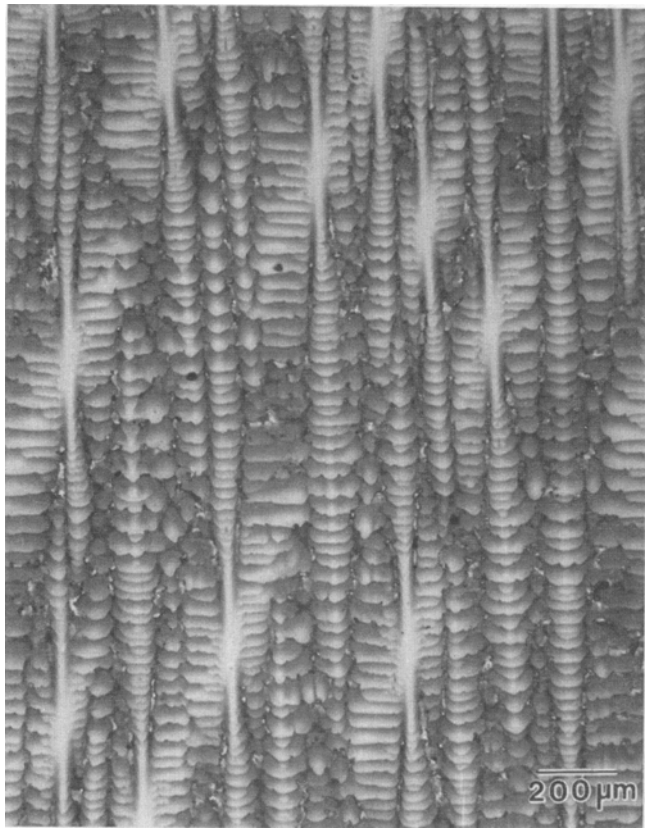

Fig. 5—A section parallel to [001] growth direction, showing secondary dendrite arms.

Table III. Results of Microprobe Analyses

Material	Al	Cr	Co	Hf	Re	Ta	W	Ni
Nominal SX1	6.0	4.5	12.5	0.16	6.3	7.0	5.8	bal
Dendrite core	5.4	4.9	13.2	0.16	9.2	5.4	6.8	bal
Interdendritic	7.6	4.4	12.2	0.13	3.4	8.2	3.9	bal
Freckle	8.2	3.6	11.0	0.18	2.3	10.0	2.9	bal

dritic region at half the spacing between two primary arms (away from the eutectic). These microprobe measurements were made on a sample with a primary dendrite arm spacing of 200 μm, with a probe analysis region of 10 μm. The segregation behavior of individual alloying elements from dendritic to interdendritic regions in this complex alloy was qualitatively consistent with the behavior expected, based on Ni-X binary phase diagrams; Re and W partitioned strongly to dendritic regions, while Ta and Al partitioned strongly to interdendritic regions.

B. *Alloy SX-1: The Breakdown of Single-Crystal Solidification*

To achieve a wide range of thermal conditions, a total of 35 casting experiments were conducted with cylinders and cluster molds. Figure 1 summarizes the imposed conditions during casting experiments. The thermal gradients during solidification were varied through changes in alloy superheat, adjustments in the configuration of radiation baffles in the furnace, and the number of samples contained on a cluster mold. Grain defects and the breakdown of single-crystal solidification were then studied in detail. A

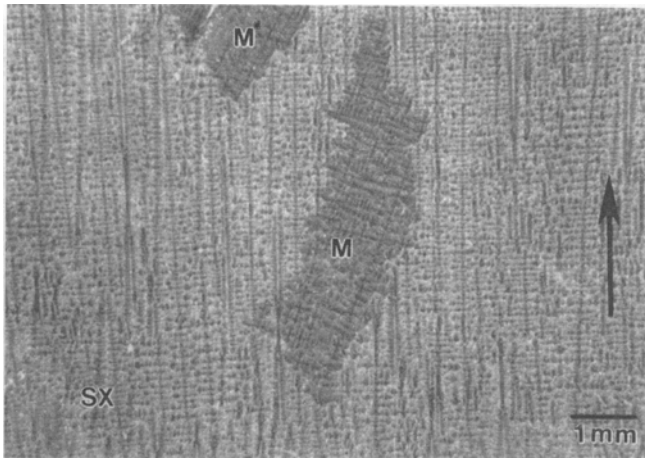

Fig. 6—Isolated columnar grains that nucleated and grew during directional solidification of alloy SX-1. The arrow indicates the growth direction. Note that the misoriented columnar grains (marked by M) are highly misoriented relative to the surrounding [001] oriented dendritic structure (marked by SX) that was present prior to grain nucleation and growth.

greater number of individual samples were examined than shown in Figure 1, since some of the experiments used cluster molds containing multiple samples arranged symmetrically around the periphery of the mold. For the blade-shaped samples, the minimum thermal gradients associated with the dovetail (base) regions of higher cross-sectional area have been listed in Figure 1. However, comparisons of thermal gradients measured by mold thermocouples and dendrite arm spacings in a large number of sections along the lengths of individual blade samples have shown that the average thermal gradients in the dovetail regions were only slightly lower, generally less than 10 pct, than in the airfoil regions. These sectioning studies also revealed very uniform primary dendrite arm spacings up to the outer edges of the casting, due to the strongly unidirectional thermal gradients. Statistical analyses showed no significant dependence of grain defect formation on the location of any individual blades on the cluster molds.

Although experiments were conducted over a wide range of imposed thermal gradients, with a maximum of 140 °C/cm in the cylinders, grain defect formation was only observed when the thermal gradients during solidification were relatively low. For alloy SX-1, no grain defects were observed when the thermal gradients were greater than approximately 15 °C/cm. For a fixed withdrawal rate, as the thermal gradients decreased below 15 °C/cm, an abrupt transition from single-crystal dendritic to equiaxed solidification was not observed. Instead, over a rather extensive intermediate regime, nucleation and growth of isolated grains occurred. Figure 6 shows a typical example of two isolated grains embedded in a crystal which predominantly consists of an [001] oriented dendritic structure (without high-angle boundaries). These grains did not immediately appear during the directional solidification process; a dendritic single-crystal region approximately 3 cm in extent solidified prior to their nucleation. From the traces of the primary dendrite trunks, it is apparent that the grains are highly misoriented relative to the [001] dendritic structure in the bulk of the material. These grains presumably assume a columnar shape due to the low nucleation density coupled

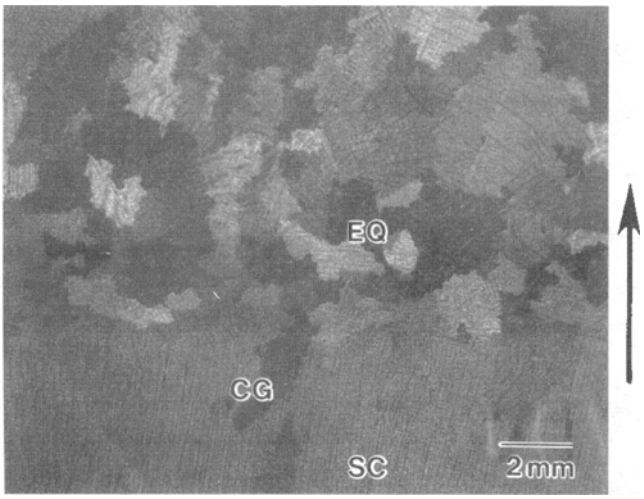

Fig. 7—Complete breakdown of single-crystal solidification and blockage of solidification front by equiaxed grains. The arrow indicates growth direction.

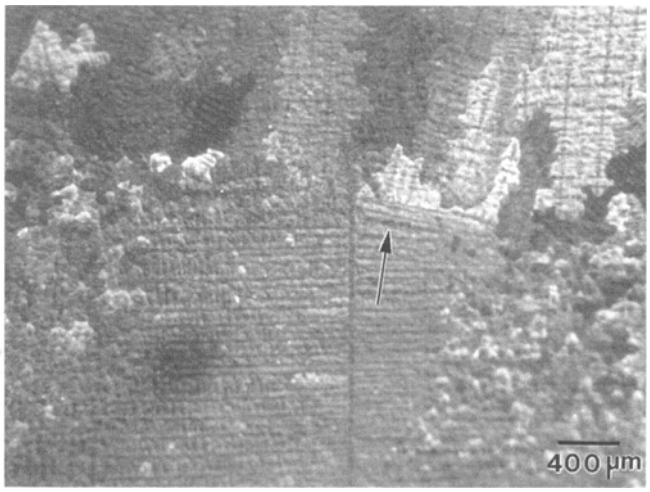

Fig. 8—Breakdown of single-crystal solidification at an airfoil-dovetail transition of a blade-shaped sample. Only one primary dendrite trunk extending from the single-crystalline region behind the transition front is present at the center of the field of view. At the arrow, a secondary dendrite arm has apparently detached and contributed to the growth of equiaxed grains at the transition.

with the presence of the positive thermal gradients and the continued unidirectional withdrawal from the hot zone of the furnace. As solidification progressed, the isolated grains were typically overgrown, permitting a return to [001] directional dendritic structure throughout the cross section of the sample. Electron microprobe analyses confirmed that the composition of these columnar grains was not significantly different from the composition of the surrounding single-crystal material. Extensive systematic sectioning studies of numerous castings through regions containing these grain defects were completed. In no cases could the formation of these grains be attributed to nucleation on inclusions in the melt. While the columnar grains were normally visible on the sample surface, occasional internal grains with no surface connections were observed.

In experiments where the thermal gradients were decreased to levels well below 15 °C/cm, greater numbers of grains were observed, until eventually a complete transition to polycrystalline solidification was reached, as shown in Figure 7. The sizes of the grains at the transition point were highly variable, but were generally in the range of 1 to 10 mm. At this transition, some of the grains were still elongated along the direction of withdrawal, but not to the extent typically observed for isolated grains. Nevertheless, the distinguishing feature was the complete blockage of the single-crystal front caused by the large-scale nucleation and growth of new grains. In Figure 8, a complete breakdown of the solidification front has occurred at the transition from a thin to a thick region (airfoil to the base) of a blade sample. Note the single primary dendrite trunk in the field of view and the apparent detachment and subsequent growth from a secondary arm at the transition front. (This primary dendrite was easily traced back into the single-crystalline region behind this transition front.) Also, near the transition, there is contrast due to the presence of very fine grains of the order of 100 μm in extent.

Figure 9 shows the number of grains observed as a function of the dendrite arm spacing for each of the experiments. From this, three regimes of behavior can be identified as a function of primary dendrite arm spacing: single-crystal (SC) solidification, solidification interrupted by occasional nucleation and subsequent growth that resulted in isolated misoriented columnar grains (CG), and "equiaxed" solidification (EQ) with complete blockage of the single-crystal front. It is interesting that there is not an abrupt transition from single-crystal growth to equiaxed solidification, but a rather large intermediate range of conditions where isolated grains nucleate and grow without completely interrupting single-crystal solidification. As shown in Figure 9, the transition from SC to CG occurred when the imposed processing conditions were such that the primary dendrite arm spacing was approximately 320 μm. Referring again to Figure 4, note that a change in dendrite morphology occurs in the same range as the transition from the SC to CG regime. When the spacing of the primary dendrites was less than approximately 320 μm, there were well-defined primary and secondary arms, but no evidence of tertiary arms, and the dendrite spacings in the cylinders, slabs, and blades were very uniform throughout the cross sections of the samples. However, as the spacing of the primary dendrites exceeded a spacing of approximately 320 μm, tertiary arms began to develop. As the gradients continued to decrease, the spacings of the primary trunks became less regular. The ultimate transition to equiaxed solidification occurred at a dendrite arm spacing of approximately 600 μm. As the primary spacings approached 600 μm, extensive coarsening and detachment and fragmentation of secondary and tertiary arms were apparent. Figure 10 shows sections transverse to the solidification direction in this range with a series of parallel secondary arms and tertiary arms that have a "necked" appearance at the joints with the secondary arms. In Figure 10(a), the secondary arms of the dendrite at the center of the micrograph show a pronounced deviation from [010] directions, and in Figure 10(b), it appears that a fragmented tertiary dendrite has rotated by approximately 45 deg within the interdendritic region, to form a new "grain."

In addition to the columnar and equiaxed grains, chains of freckle-type defects were also observed in some of the experiments in the low gradient regime. One example of a

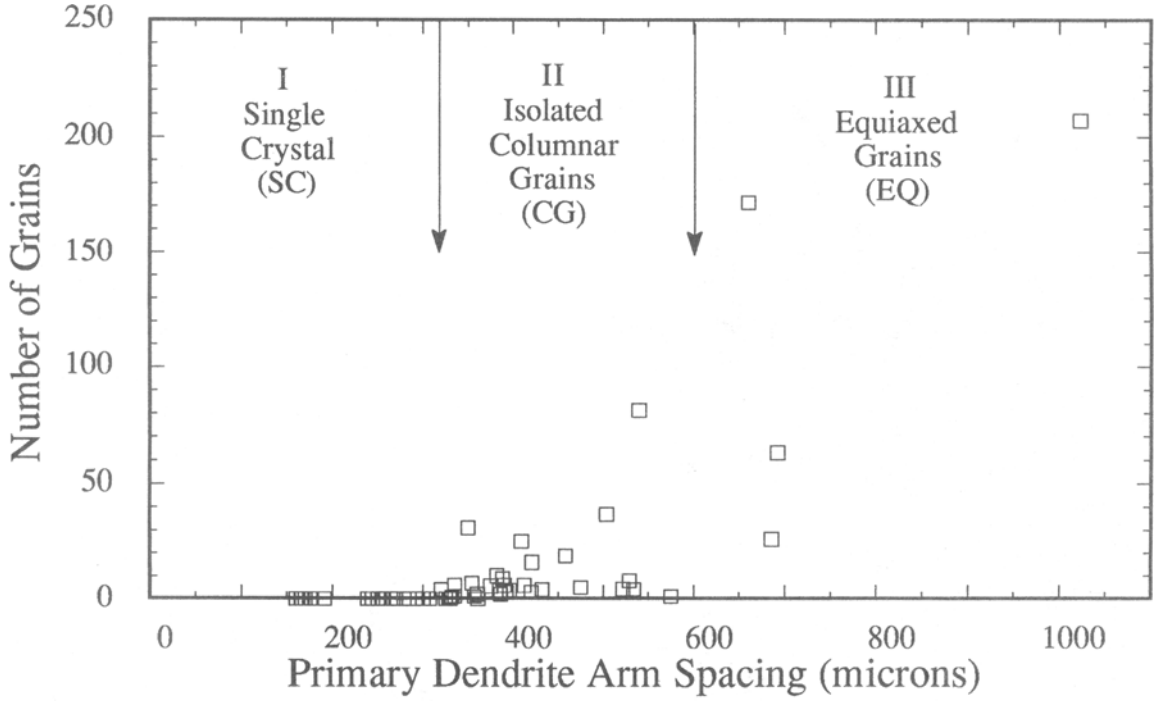

Fig. 9—The number of columnar or equiaxed grains observed in experiments conducted over a wide range of thermal gradients and withdrawal rates. Note the three distinct regimes of solidification behavior as a function of dendrite arm spacing.

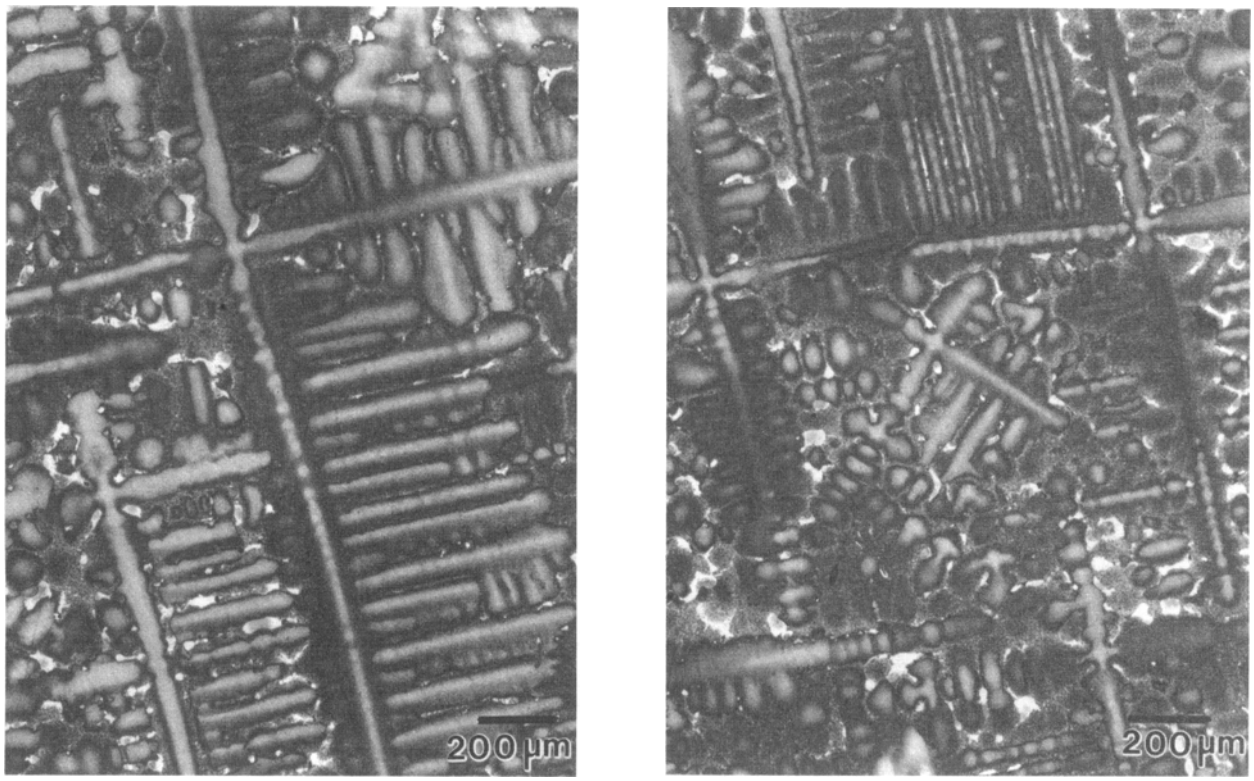

(*a*) (*b*)

Fig. 10—Sections normal to solidification direction under conditions near the transition to equiaxed solidification. Tertiary arms appear to be separated from secondary arms, and (*a*) the long secondary arm displays a pronounced curvature, while (*b*) an isolated dendrite fragment (at center) is rotationally misoriented by approximately 45 deg.

freckle chain is shown in Figure 11. Unlike the larger columnar and equiaxed grains, the composition of the freckles varied from the base material composition. These grains were enriched in the elements that are rejected to interdendritic regions during solidification. Note in Table III that the composition of the freckles was similar to the compo-

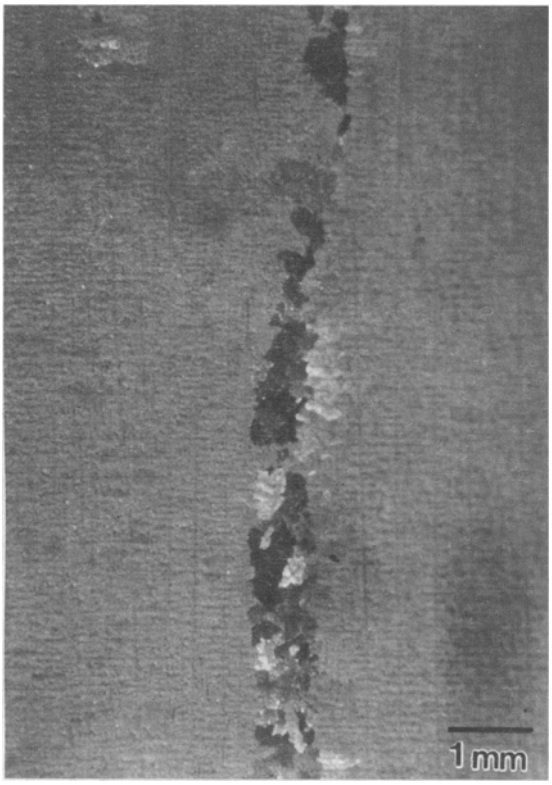

Fig. 11—A typical freckle chain observed during solidification of alloy SX-1.

sition of the interdendritic regions, with enrichment in Al and Ta, and strong depletion of Re and W, relative to the base composition. The equiaxed grains within the freckle chains were usually in the range of 200 to 1000 μm, which is much smaller than that of the columnar grains. In Figure 12, the number of freckle chains as a function of primary dendrite arm spacing is shown. Interestingly, there is again a transition at a dendrite arm spacing of approximately 320 μm, indicating an important role of convection in the development of both freckles and columnar grains. This will be discussed in more detail in Section IV.

C. *The Influence of Alloy Composition*

The compositions of the ten alloys studied are listed in Table I. The contribution of refractory alloying additions to the breakdown of solidification was of primary interest, so large variations in Re, Ta, and W content were investigated. Smaller variations in Cr, Al, Co, and Hf were also investigated. All experiments were conducted with blade-type samples with a fixed withdrawal rate of 0.0113 cm/s and thermal gradients in the airfoil section of approximately 10 °C/cm. For alloy SX-1, these conditions resulted in a primary dendrite arm spacing of 307 μm, which is at the threshold of the SC to CG transition. By selecting these conditions, the role of solute in suppressing or enhancing grain defect formation could be studied in the vicinity of the transition. No transitions to completely equiaxed solidification were induced by the changes in composition investigated here.

Figure 13(a) shows the average number of columnar grains formed per blade sample (out of a total of seven samples) for each of the alloys investigated. Similarly, Figure 13(b) shows the average number of freckle chains per blade sample. From these figures, it is apparent that the formation of both freckles and columnar grains is sensitive to the Ta content and, to a lesser extent, Re and W. Few defects formed in alloys 7 through 10, which contained higher Ta levels compared to alloys 1 through 6. Figures 14(a) and (b) show the 95 pct confidence intervals associ-

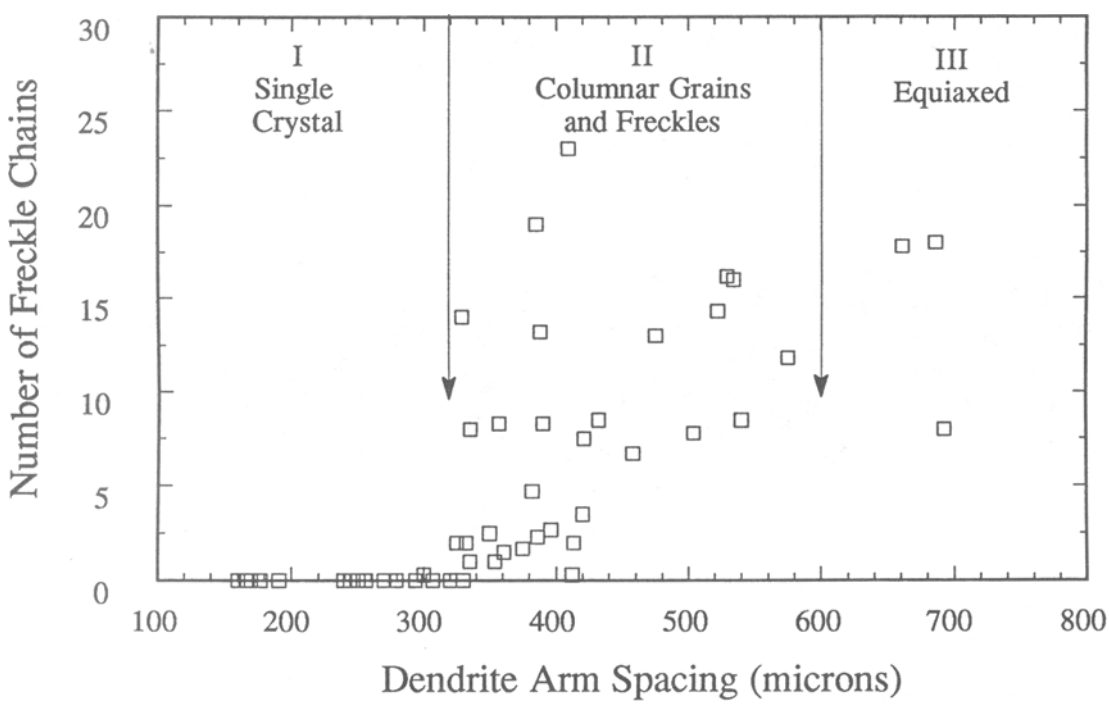

Fig. 12—The dependence of freckle chain formation on primary dendrite arm spacing. Note that the onset of freckle formation occurs under the same conditions as for the misoriented grains (Fig. 9).

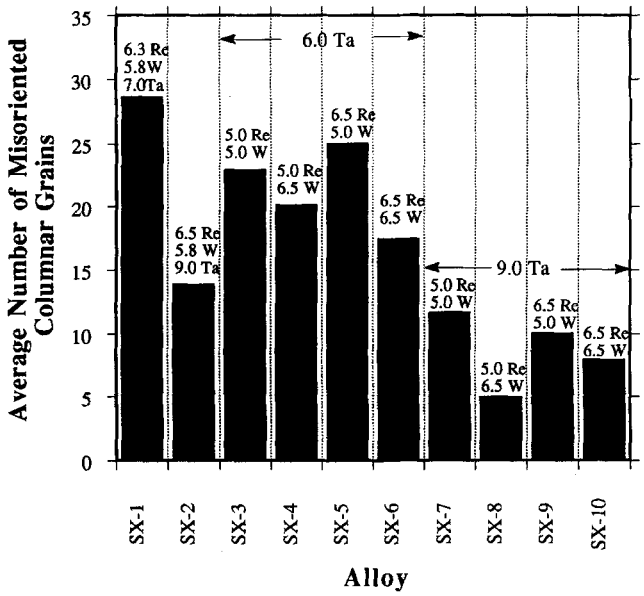

(*a*)

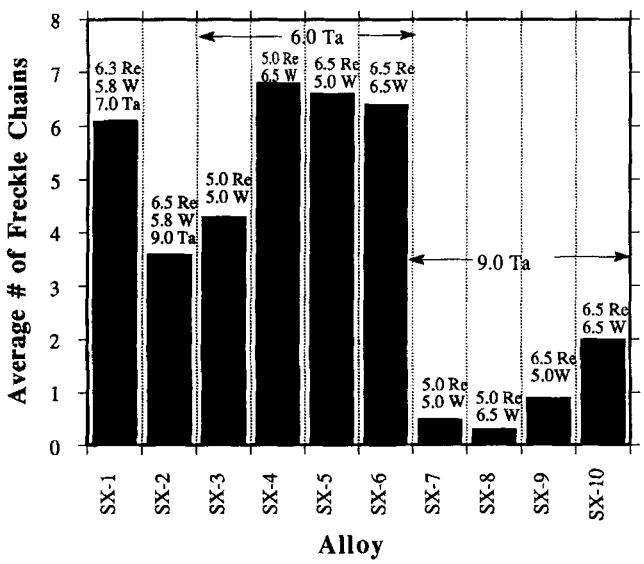

(*b*)

Fig. 13—The dependence of (*a*) columnar grain and (*b*) freckle chain formation on alloy chemistry.

ated with the mean number of defects in each alloy as well as a comparison of the means. From this, it is clear that higher levels of Ta are effective in suppressing the formation of both freckles and columnar grains, while the effects of Re and W are weaker. The correlation between the number of misoriented columnar grains and freckle chains is shown in Figure 15. No statistically significant variations in the tendency for defect formation could be attributed to changes in the levels of Al, Cr, Co, or Hf or interstitial elements within the ten alloys.

To check for any unusual changes in the freezing range of the alloys associated with this range of chemistry, differential thermal analyses were completed, and the results are given in Table II. No correlation between defect formation and the solidus, liquidus, or freezing ranges of the alloys was apparent.

Compared to alloy SX-1, discussed in Section B, no significant differences in the dendrite arm spacings or dendrite

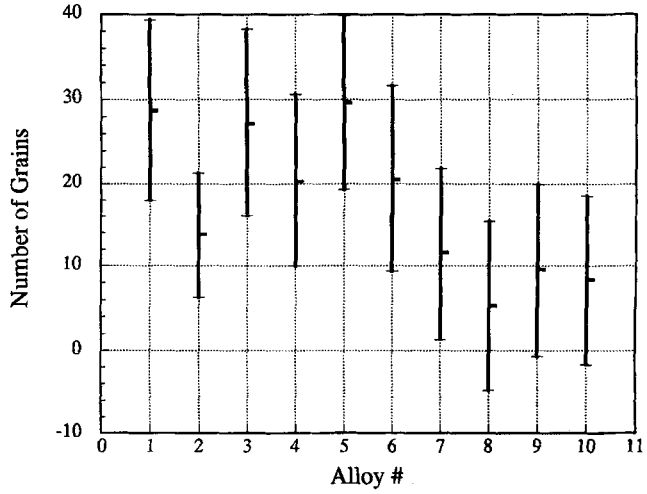

(*a*)

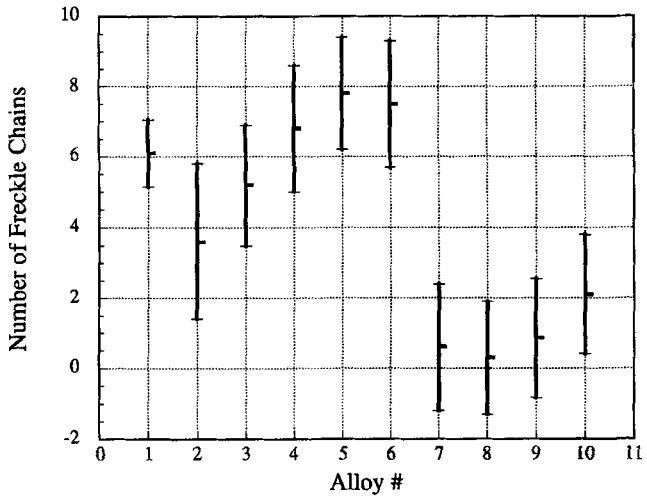

(*b*)

Fig. 14—The mean number of (*a*) columnar grains and (*b*) freckle chains as a function of alloy composition and the associated 95 pct confidence intervals.

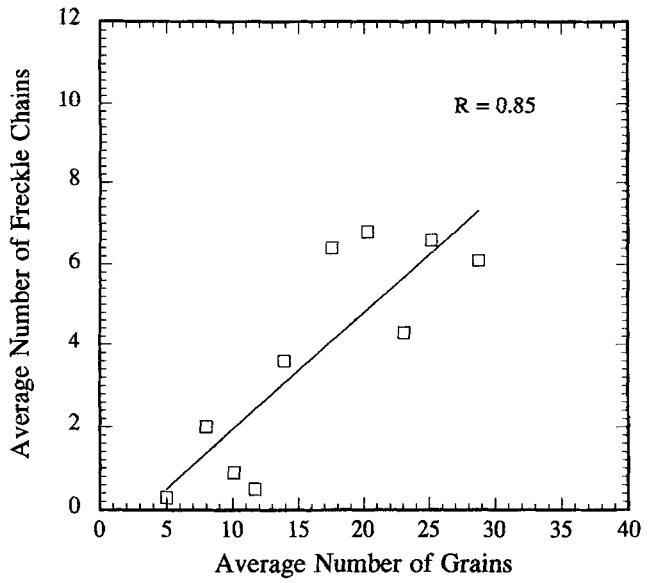

Fig. 15—The correlation between the number of columnar grain and freckle chain defects observed in experiments on the ten experimental alloy compositions near the single-crystal to columnar grain transition.

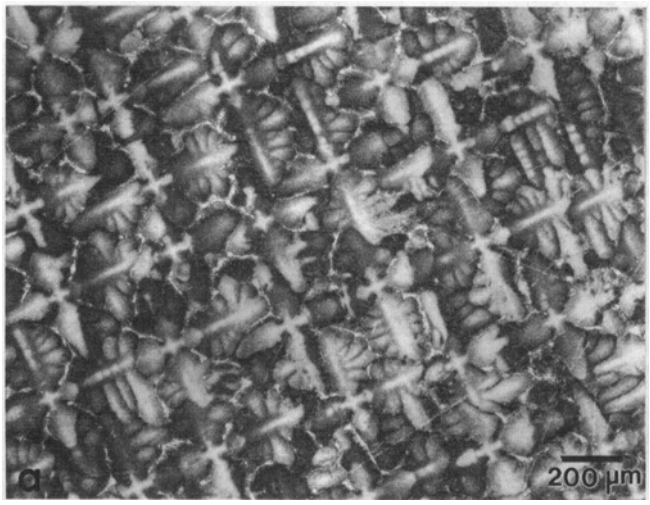

(*a*)

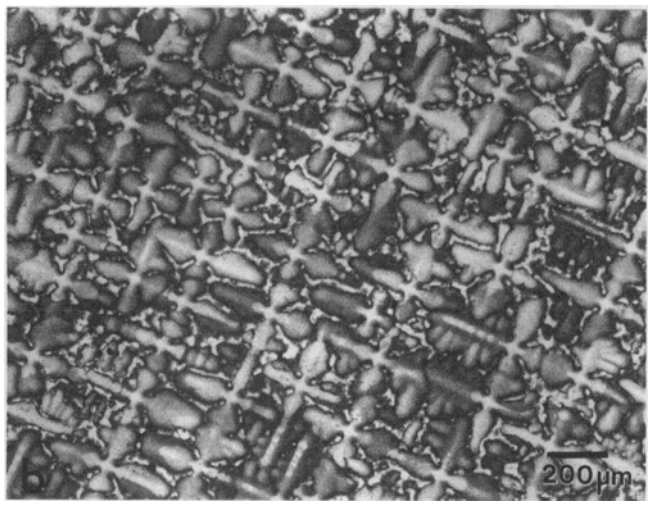

(*b*)

Fig. 16—Dendrite morphology normal to growth direction in alloys (*a*) SX-3 and (*b*) SX-6, solidified near the SC to CG transition.

morphologies were noted with variations in alloy chemistry. Figure 16 shows the dendritic structure in sections normal to the solidification direction for alloys SX-3 and SX-6. In both cases, tertiary arms have developed, as expected, since the imposed solidification conditions were near the SC to CG transition.

IV. DISCUSSION

Over the range of experimental conditions investigated, the breakdown of single-crystal solidification was sensitive to local thermal *and* solutal conditions. For a fixed alloy composition, the onset of grain defect formation occurred when the primary dendrite arm spacing exceeded a critical value, corresponding to a morphological transition in the dendritic array. For alloy SX-1, the onset of freckling was also observed at the same primary dendrite arm spacing where isolated grains began to nucleate and grow. In experiments where the refractory alloy content was varied, there was also a correlation between the onset of columnar grain formation and freckle formation. These observations strongly suggest that the breakdown of single-crystal solidification and the development of the isolated misoriented grains as well as freckle-type defects are dependent on thermosolutal convection.

Although the onset of isolated grain nucleation during directional solidification has not been studied in detail to date, the formation of freckle-type defects has been studied extensively in transparent compounds,[8] Pb-Sn alloys,[9] and nickel-base alloys.[7] As solute is rejected during unidirectional solidification of these materials, large density inversions develop in the interdendritic fluid, resulting in convective flow and the formation of solute-rich channels.[17] With a sufficiently high fluid velocity, dendrite dissolution and fragmentation can occur.[8]

In the alloys studied here, freckles rich in elements that segregate to the interdendritic fluid have been observed. Dendrite detachment was also apparent, especially in experiments where the thermal gradients were low and the primary dendrite arm spacings large. Since the onset of columnar grain formation and freckling occur under the same thermal and solutal conditions, and there is even a reasonable correlation between the *numbers* of these defects, it is likely that convection and dendrite detachment and fragmentation contribute to the development of large, columnar grains as well as freckle-type defects, and ultimately to the transition to polycrystalline equiaxed solidification.

From Figures 9 and 12, it is clear that the transition from single-crystal dendritic solidification to equiaxed solidification was not abrupt. Instead, over an intermediate range of conditions where positive thermal gradients persisted at the solidification front, occasional misoriented grains were observed. As the thermal gradients were reduced to very low levels, greater numbers of grains nucleated and grew until the density of the newly nucleated grains became sufficiently high to completely block the advance of the single-crystal solidification front. The development of the isolated columnar grains over the intermediate range of conditions (where positive unidirectional gradients persist) may be limited to a greater degree by either the detachment and fragmentation processes or by the subsequent growth processes. One possibility is that fragmented secondary or tertiary arms become entangled in the advancing dendritic front. Under these conditions, the survival and subsequent growth of the reoriented fragment would be dependent on the thermal gradient, which would govern the rate of dissolution, and the solidification rate, that would limit the time available for dissolution. Considering this, low gradients and high solidification rates would promote *growth* of the fragment into a misoriented grain. The would suggest that below some critical level of G/R, nucleation and subsequent growth of misoriented columnar grains would be possible. Clearly, a more detailed consideration of the kinetics of the dissolution process with the presence of a positive thermal gradient and an advancing interface is needed. However, as discussed further in Section A, the limiting phenomenon may instead be the convection-driven detachment and fragmentation processes at the solidification front. In this case, different macroscopic criteria for the breakdown of solidification are required.

A. *The Role of Solute*

The equation of motion for an element of fluid during solidification is given by the Navier–Stokes equation:

Table IV. Approximate Distribution Coefficients for Alloy SX-1

Material	Al	Cr	Co	Hf	Re	Ta	W	Ni
Alloy SX-1	0.91	1.09	1.06	—	1.47	0.77	1.17	0.94

$$\rho\left(\frac{\partial \mathbf{u}}{\partial t} + \mathbf{u}\cdot\nabla\mathbf{u}\right) = \rho f - \nabla p + \nabla(\eta\nabla\mathbf{u}) \qquad [2]$$

where $\mathbf{u}$ is the fluid velocity (a vector quantity), ρ is the fluid density, p is pressure, η is viscosity, and f is the force exerted on a volume element due to the thermal and concentration gradients. For unidirectional solidification, the upward buoyancy force due to thermal and concentration gradients is[18]

$$f_z = -g\rho\,(\beta_T[T - T^*] + \beta_c[C - C^*]) \qquad [3]$$

where

$$\beta_T = -\left(\frac{\partial \ln \rho}{\partial T}\right)_C \qquad [4]$$

$$\beta_c = -\left(\frac{\partial \ln \rho}{\partial C}\right)_T \qquad [5]$$

The values T^* and C^* are the average temperature and concentration, respectively, and g is the gravitational constant. Obtaining an analytical solution to Eq. [2] for the convective processes observed here is not possible, due to the complex nature of the dendritic array and the associated boundary conditions. Nevertheless, under the unidirectional solidification conditions studied here, convection in the melt should occur when the density gradient due to the simultaneous temperature and concentration gradients exceeds a critical value.[19] Although information on liquid density as a function of refractory element content is not available, the elements which influence defect formation to the greatest extent, Re, W, and Ta, all have atomic masses 3 times that of nickel in the solid state. It is therefore essential to control the levels of the elements present as well as to understand their partitioning behavior during solidification.

For a high Ta single-crystal superalloy, Tewari *et al.*[20] have characterized microsegregation in detail and measured distribution coefficients. Their data suggested that during solidification of single-crystal superalloys, the assumptions of limited solid diffusion and rapid liquid diffusion are reasonable. Assuming the same for the alloys investigated here, the data for the composition of the solid in the dendrite cores (Table III) can be used to obtain a rough estimate of the distribution coefficients of the individual alloying elements in alloy SX-1. With a primary dendrite arm spacing of 200 μm and a probe analysis region of 10 μm, the composition listed in Table III should represent the average composition over the interval of $f_s = 0$ to $f_s = 10/200 = 0.05$, where f_s is the fraction solid. Assuming the Scheil equation is applicable to the segregation of individual elements, then an approximate distribution coefficient, k, can be obtained from the average composition of solid $\bar{C}_s$ forming from $f_s = 0.0$ to $f_s = 0.05$ as

$$\bar{C}_S = \int_0^{0.05} \frac{kC_0\,(1 - f_s)^{k-1}\,df_s}{0.05} \qquad [6]$$

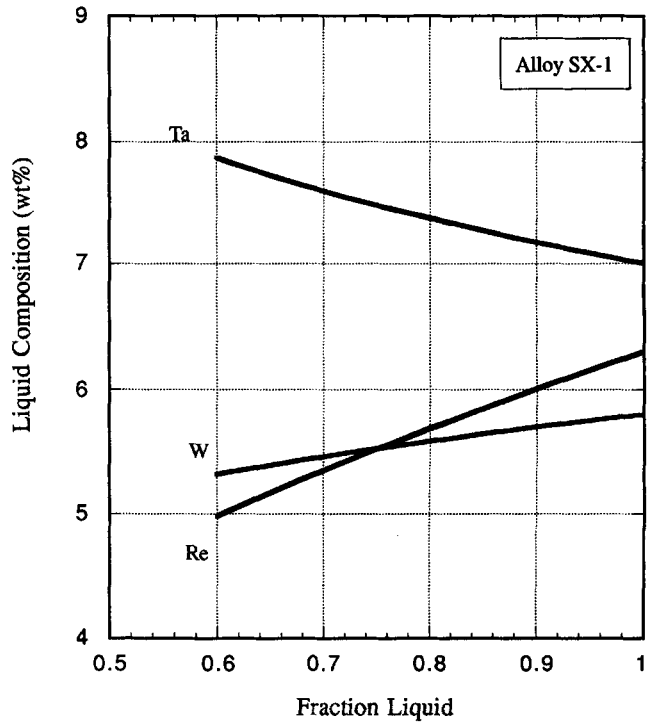

Fig. 17—Approximate distribution of Ta, Re, and W in the mushy zone during solidification. The Ta enrichment can offset the depletion of Re and W, reducing the probability of convection-induced defect formation.

where C_0 is the amount of solute in the bulk alloy. The approximate distribution coefficients obtained from this analysis are listed in Table IV. It should be emphasized that these coefficients, and in particular those for relatively rapidly diffusing elements such as Al and Cr, may be influenced by solid-state diffusion during the subsequent withdrawal process. The Ta, Re, and W, in addition to being the elements with the highest atomic mass, are also the most strongly partitioning elements. With these distribution coefficients, the variation in their content in the liquid (assuming no convection) in the upper region of the mushy zone is shown in Figure 17. From the point of view of minimizing the driving force for convection, progressive Ta enrichment is clearly desirable, in order to offset density decreases caused by depletion of Re and W as the alloy progressively solidifies. This is consistent with the lower numbers of defects present in samples containing 9 pct Ta, compared to those containing 6 pct (Figures 13(a) and (b)).

Sarazin and Hellawell[9] considered the development of convective instabilities in terms of dimensionless thermal and solutal Rayleigh numbers. However, considering the large primary arm spacings and the dendrite fragmentation processes which apparently contribute to grain defect formation for the high refractory content nickel-base alloys studied here, it is likely that the permeability of the dendritic network influences the breakdown of solidification. Horton and Rogers[21] and Wooding[22] have considered convective instabilities in porous media. For a network of permeability K in a unidirectional temperature gradient, the relevant Rayleigh number is

$$R_T = \frac{g\alpha\left(\frac{dT}{dz}\right)Kh^2}{\eta\kappa} \qquad [7]$$

where g is the gravitational constant, α is the volume coefficient for thermal expansion, η is viscosity, κ is thermal diffusivity, and h is the characteristic length of the porous medium. Note that in a porous network, the sensitivity to the characteristic length, h, is reduced, since the dependence of h^4 in the original analysis of Rayleigh is replaced by Kh^2.

Extending this to consider the role of solute segregation, a Rayleigh solute number may also be considered:

$$R_S = \frac{g\beta\left(\frac{dC_L}{dz}\right)Kh^2}{\eta D} \quad [8]$$

where D is diffusivity and β is the solute volume expansion coefficient. In the directional solidification process considered here, the thermal gradients are positive and stabilizing. It is then of interest to consider how solute can result in instability *via* consideration of Eq. [8]. Following the argument of Kurz and Fisher,[13] and assuming that the outer envelope of the dendrite can be approximated by an ellipsoidal shape with minor and major axes of b and h, respectively, the dendrite tip radius, r, is given by

$$r = \frac{\lambda^2}{3h} \quad [9]$$

where the primary dendrite arm spacing is λ. Also, since $\frac{dC_L}{dz} = \frac{G}{m_L}$,

$$R_S = \frac{g\beta G}{9r^2\eta m_L}\left(\frac{K\lambda^4}{D}\right) \quad [10]$$

From this, it is clear that the development of convection-induced grain defects will be enhanced in high permeability dendritic networks with large primary dendrite arm spacings. Although there is little information regarding the permeability of dendritic networks in the materials of interest here, the results in Figures 9 and 12 indicate a high sensitivity of defect formation to the primary dendrite arm spacing. Further, substituting the relationship between dendrite arm spacing and G, R gives

$$R_S = \frac{g\beta\phi}{9r^2\eta m_L D}\left(\frac{K}{GR}\right) \quad [11]$$

where ϕ is the set of material parameters which relate to primary spacing selection.[13,14] Again, it is clear that low cooling rates (relatively low thermal gradients) will promote the breakdown of single-crystal solidification. It should be emphasized that low cooling rates, achieved through very high thermal gradients and low solidification rates, would not produce the same morphological instabilities in the dendritic network, and therefore are less likely to lead to nucleation of grain defects through fragmentation processes.

B. *Implications for Macroscopic Grain Defect Criteria*

From a technological point of view, it is desirable to define macroscopic single-crystal processing conditions as well as alloying additions which can prevent formation of grain defects in single-crystal castings. Recent solidification modeling efforts[23,24] have focused on the definition of boundary conditions and description of macroscopic heat flow conditions. With this information, regions of a casting that are prone to defect formation can be identified by use of macroscopic grain defect criteria that ideally relate to the operative microscopic phenomena. Unfortunately, a number of difficulties arise in selecting criteria for the prediction of grain defect formation during single-crystal solidification. First, it is either necessary to account for all possible grain nucleation mechanisms or to identify alloys/regimes were one mechanism dominates. Here, solute-induced convective instabilities and their influence on dendrite detachment and fragmentation are key to grain "nucleation." The second requirement is to establish the conditions under which nuclei subsequently grow into columnar or equiaxed grains. In terms of thermal gradients and solidification rates, a single criterion for this series of events may not apply. Another complication is the difficulty of relating approximate thermal gradients and solidification rates, as measured here, to the local conditions at the front at any given time during solidification. Detailed modeling of the local conditions is presently very difficult, due to the complicated morphology and permeability of the dendritic network and the presence of thermosolutal convection. However, it appears that it is essential to include convection in any comprehensive solidification model that addresses grain defect formation at the microscopic level. Nevertheless, to explore whether additional macroscopic criteria are appropriate for alloys and/or solidification conditions where convection-induced defect formation dominates, it is informative to compare the present experimental results to the various macroscopic criteria that have been proposed for the transition to equiaxed solidification.

Copley *et al.*[7] proposed that a transition to equiaxed solidification during unidirectional solidification occurs when more heat is released into the mushy zone that can be conducted away through the solid at a critical level of (G/R). Alternatively, the theory of Hunt[3] proposes that a transition will occur at a critical gradient, when grains nucleate heterogeneously in advance of the solidification front. Under conditions where no solute-induced convective instabilities were present, Mahapatra and Weinberg[25] observed a transition from columnar grain solidification to equiaxed at a critical thermal gradient in Pb-Sn alloys. Since single crystals were not used in those experiments, the onset of isolated columnar grain formation could not have been observed, as was the case in this work. The onset of channel formation and freckling is alternatively thought to occur at a critical local solidification time (inversely proportional to G^*R) or a critical effective Rayleigh number, and therefore $G^{-1/2}R^{-1/4}$.[9,12] In Figures 18 through 21, are the number of grains observed as a function of G, G/R, G^*R, and $G^{-1/2}R^{-1/4}$, respectively. From these figures, it is apparent that the critical G or the G/R criteria are not sufficient at lower levels of G or G/R. For example, above a critical gradient of approximately 15 °C/cm, there are no grain defects. However, for a gradient of 10 °C/cm, there were several experiments in which there was no grain defect formation, but also two experiments where grain nucleation and growth did occur. Referring again to Figure 21, it is clear that a critical level of $G^{-1/2}R^{-1/4} = 0.95$ cm$^{1/4}$ s$^{1/4}$ °C$^{-1/2}$ best defines the onset of grain defect formation.

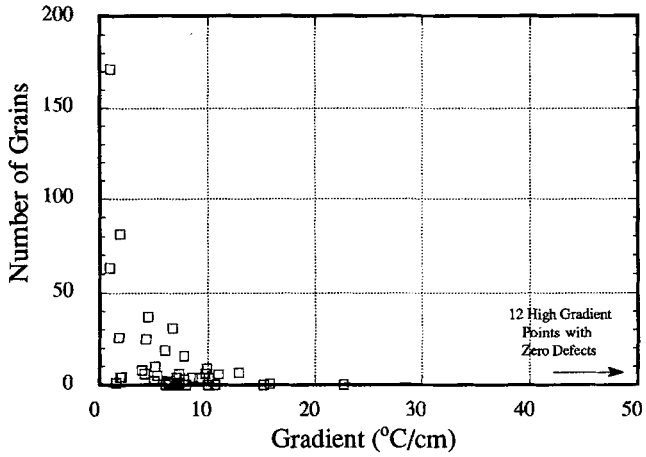

Fig. 18—The number of columnar or equiaxed grains present as a function of imposed thermal gradients in alloy SX-1 experiments.

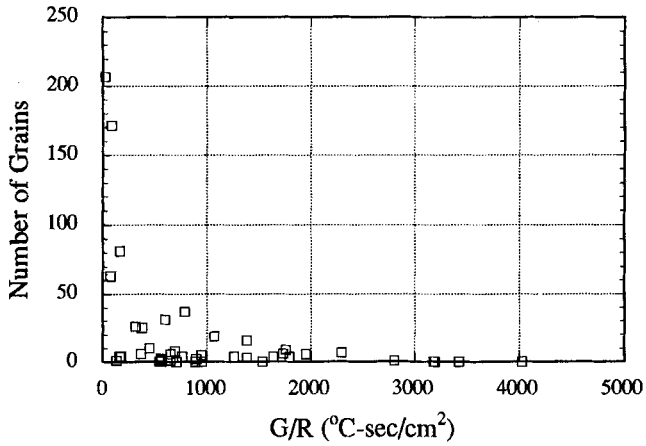

Fig. 19—The number of columnar or equiaxed grains present as a function of imposed *G/R* in alloy SX-1 experiments.

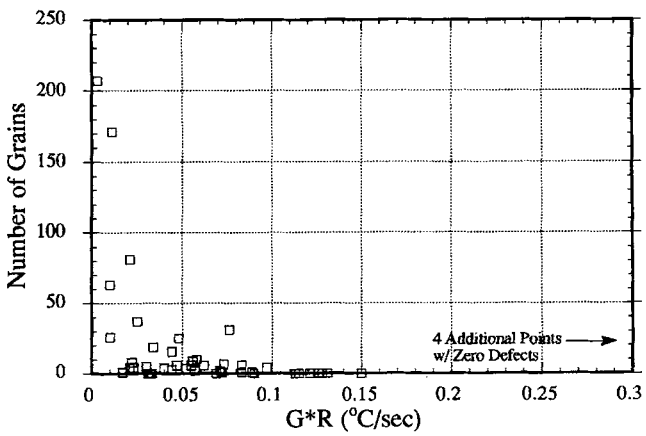

Fig. 20—The number of columnar or equiaxed grains present as a function of imposed cooling rate in alloy SX-1 experiments.

Beyond this, there is only one anomalous experiment with no grain defects; the reasons for this are not clear. Note also in the composite plot of Figure 22 that the onset of freckle formation occurs at approximately the same conditions, which is not surprising considering that defect formation showed a strong correlation with primary dendrite arm spacing (Figures 9 and 12). The composite plot in Figure 22 summarizes all of the criteria relative to the presence

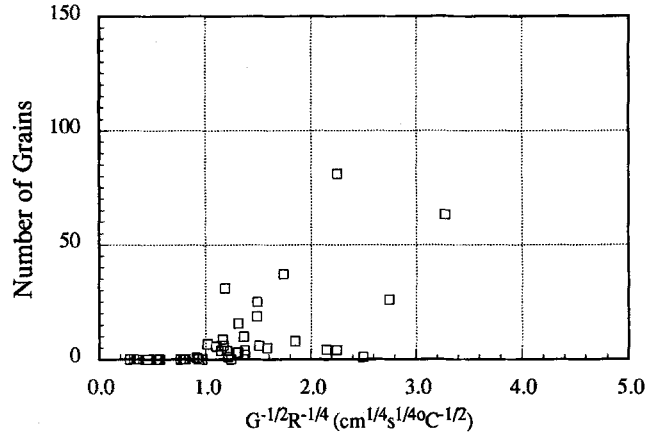

Fig. 21—The number of columnar or equiaxed grains present as a function of $G^{-1/2}R^{-1/4}$ in alloy SX-1 experiments.

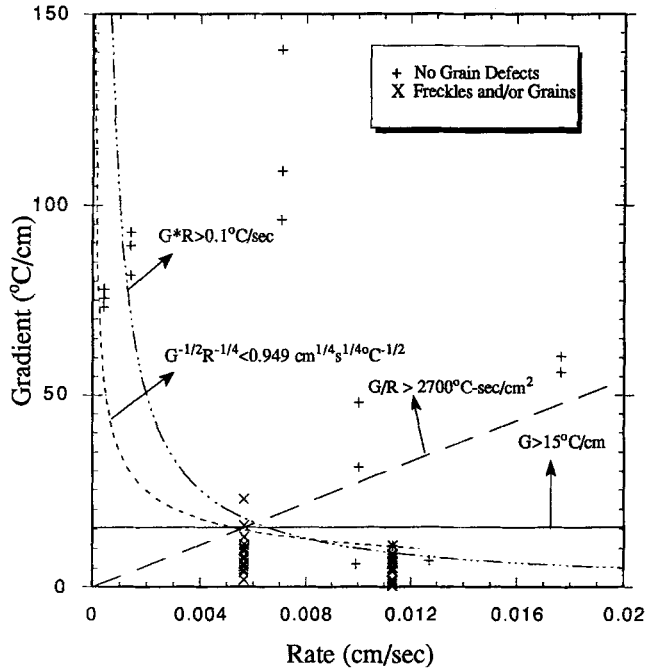

Fig. 22—Combined comparison of macroscopic criteria for grain defect formation in single-crystal solidification for alloy SX-1.

of the defects. Use of critical *G*, *G/R*, or *G*R* criteria may be unnecessarily conservative. Also, from Figure 22, it is evident that a greater number of experiments would be useful for further critical evaluation of defect criteria.

V. CONCLUSIONS

1. For the high-refractory alloy SX-1, the transition from dendritic single-crystal to equiaxed solidification occurs gradually, with an intermediate regime in which isolated grains nucleate and subsequently grow to columnar shapes in the presence of positive (stabilizing) thermal gradients.
2. The onset of isolated columnar grain formation and freckle formation occurred at the same critical primary dendrite arm spacing in alloy SX-1, suggesting that thermosolutal convection promotes the development of both types of defects.
3. Grain defect formation was sensitive to the level of Ta, Re, and W contained in an alloy. Density inversions can be

minimized by maintaining high levels of Ta, which is progressively rejected to interdendritic regions as Re and W are depleted.

4. At very low thermal gradients, sufficient numbers of grains nucleate at the solidification front to completely block the advance of the solidification front. Remelting, detachment and fragmentation of secondary and tertiary arms contribute to this process.

ACKNOWLEDGMENTS

The authors are grateful to D. Kirch and M. Cannon for their assistance with sample preparation and microprobe analyses. The authors would also like to acknowledge useful discussions with S.C. Huang, E.G. Goldman, R.A. McDaniel, F. Gruber, D.L. Uram, and J.S. Tu. The support of the General Electric Company is gratefully acknowledged, and one author (TMP) would also like to acknowledge the support of NSF-NYI Grant No. DMR-9258297.

REFERENCES

1. B. Chalmers: *J. Aust. Inst. Metall.*, 1963, vol. 8, pp. 255-61.
2. W.C. Winegard and B. Chalmers: *Trans. ASM*, 1954, vol. 46, pp. 1214-22.
3. J.D. Hunt: *Mater. Sci. Eng.*, 1984, vol. 65, pp. 75-83.
4. K.A. Jackson, J.D. Hunt, D.R. Uhlmann, and T.P. Seward: *Trans. AIME*, 1966, vol. 236, pp. 149-58.
5. C.Y. Wang and C. Beckermann: *Metall. Trans. A*, 1994, vol. 25A, pp. 1081-93.
6. Ch.-A. Gandin and M. Rappaz: *Acta Metall. Mater.*, 1994, vol. 42, pp. 2233-46.
7. S.M. Copley, A.F. Giamei, S.M. Johnson, and M.F. Hornbecker: *Metall. Trans.*, 1970, vol. 1, pp. 2193-2204.
8. A.F. Giamei and B.H. Kear: *Metall. Trans.*, 1970, vol. 1, pp. 2185-92.
9. J.R. Sarazin and A. Hellawell: *Metall. Trans. A*, 1988, vol. 19A, pp. 1861-71.
10. T.M. Pollock, W.H. Murphy, E.H. Goldman, D.L. Uram, and J.S. Tu: in *Superalloys 1992*, S.D. Antolovich, R.W. Stusrud, R.A. MacKay, D.L. Anton, T. Khan, R.D. Kissinger, D.L. Klarstrom, eds., TMS, Warrendale, PA, 1992, pp. 125-34.
11. T.M. Pollock and A.S. Argon: *Acta Metall. Mater.*, 1992, vol. 40, pp. 1-30.
12. T.M. Pollock: *Mater. Sci. Eng.*, 1995, vol. B32, pp. 255-66.
13. W. Kurz and D.J. Fisher: *Acta Metall.*, 1981, vol. 29, pp. 11-20.
14. J.D. Hunt: *Solidification and Casting of Metals*, Metals Society, London, 1979.
15. P.N. Quested and M. McLean: *Mater. Sci. Eng.*, 1984, vol. 65, pp. 171-80.
16. G.K. Bouse and J.R. Mihalisin: in *Superalloys, Supercomposites and Superceramics*, J.K. Tien and T. Caulfield, eds., Academic Press, Boston, MA, 1988, pp. 99-148.
17. N. Streat and F. Weinberg: *Metall. Trans.*, 1974, vol. 5, pp. 2539-48.
18. W.A. Tiller: *The Science of Crystallization*, Cambridge University Press, Cambridge, 1991.
19. S.R. Corriell, M.R. Cordes, W.J. Boettinger, and R.F. Sekerka: *J. Cryst. Growth*, 1980, vol. 49, pp. 13-28.
20. S.N. Tewari, M. Vijaya Kumar, J.E. Lee, and P.A. Curreri: NASA TM-103518, 1990.
21. C.W. Horton and F.T. Rogers: *J. Appl. Phys.*, 1945, vol. 16, pp. 367-70.
22. K.A. Wooding: *Proc. R. Soc. London*, 1959, vol. A252, pp. 120-34.
23. K.O. Yu, J.A. Oti, M. Robinson, and R.G. Carlson: in *Superalloys 1992*, S.D. Antolovich, R.W. Stusrud, R.A. MacKay, D.L. Anton, T. Khan, R.D. Kissinger, and D.L. Klarstrom, eds., TMS, Warrendale, PA, 1992, pp. 135-44.
24. J.S. Tu and R.K. Foran: *JOM*, 1992, vol. 44, pp. 26-29.
25. R.B. Mahapatra and F. Weinberg: *Metall. Trans. B*, 1987, vol. 18B, pp. 425-32.